

General Kinetic Model for pH Dependence of Proton-Coupled Electron Transfer: Application to an Electrochemical Water Oxidation System

Kai Cui, Alexander V. Soudackov, Matthew C. Kessinger, Jeremiah Xu, Gerald J. Meyer, and Sharon Hammes-Schiffer*



Cite This: *J. Am. Chem. Soc.* 2023, 145, 19321–19332



Read Online

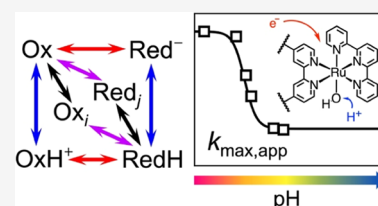
ACCESS |

Metrics & More

Article Recommendations

Supporting Information

ABSTRACT: The pH dependence of proton-coupled electron transfer (PCET) reactions, which are critical to many chemical and biological processes, is a powerful probe for elucidating their fundamental mechanisms. Herein, a general, multichannel kinetic model is introduced to describe the pH dependence of both homogeneous and electrochemical PCET reactions. According to this model, a weak pH dependence can arise from the competition among multiple sequential and concerted PCET channels involving different forms of the redox species, such as protonated and deprotonated forms, as well as different proton donors and acceptors. The contribution of each channel is influenced by the relative populations of the reactant species, which often depend strongly on pH, leading to complex pH dependence of PCET apparent rate constants. This model is used to explain the origins of the experimentally observed weak pH dependence of the electrochemical PCET apparent rate constant for a ruthenium-based water oxidation catalyst attached to a tin-doped In_2O_3 (ITO) surface. The weak pH dependence is found to arise from the intrinsic differences in the rate constants of participating channels and the dependence of their relative contributions on pH. This model predicts that the apparent maximum rate constant will become pH-independent at higher pH, which is confirmed by experimental measurements. Our analysis also suggests that the dominant channels are electron transfer at lower pH and sequential PCET via electron transfer followed by fast proton transfer at higher pH. This work highlights the importance of considering multiple competing channels simultaneously for PCET processes.



INTRODUCTION

Proton-coupled electron transfer (PCET) reactions are ubiquitous and crucial steps in chemical, biological, and catalytic processes.^{1–11} Understanding the mechanistic details of PCET reactions can allow control of these processes. A powerful mechanistic probe is the pH dependence of PCET reaction rates in aqueous solution. For example, a pH-independent apparent rate constant often indicates either a sequential mechanism with rate-limiting electron transfer (ET) or a concerted mechanism with H_2O as the proton donor or acceptor.¹² If the apparent rate constant k increases or decreases 10-fold per pH unit, H_3O^+ or OH^- are often assumed to be the sole proton donor or acceptor, and a plot of $\log k$ versus pH should have a slope of ± 1 . However, in several studies, a much weaker pH dependence of the PCET apparent rate constant has been observed. These examples include the homogeneous oxidation of tyrosine^{13–15} and tryptophan,^{16–18} as well as the interfacial reduction of Ru-based water oxidation catalysts.¹⁹ However, an explanation for these weak pH dependencies remains elusive. Herein, we will show that the weak pH dependence of some PCET reactions can be explained in terms of a competition among multiple mechanisms.

The idea of competing reactions has a long history in the PCET literature.^{12,20–23} Laviron developed a model to

describe the pH dependence of the apparent standard rate constant for stepwise, electrochemical PCET reactions.²⁰ In this model, the competition between two ET reactions involving the protonated or deprotonated redox species is considered. The resulting pH-dependent standard rate constant has two plateaus at low and high pH limits connected by a V-shape curve.²⁰ In the intermediate pH region, the rate constant first decreases due to the depletion of the protonated form and then increases due to the growing contribution from the deprotonated form, resulting in the V-shape curve. This model was then generalized by Finklea²¹ to stepwise multi-proton multi-electron PCET reactions. In addition to the stepwise case, recently, the Surendranath group developed a model that considers the competition between two concerted pathways with different proton donors on a graphitic conjugated catalyst interface.²² The predicted pH-dependent apparent standard rate constant also has a V-shape, which

Received: May 26, 2023

Published: August 23, 2023



agrees with the experimental results. All of these models were developed for electrochemical PCET reactions and rely on the Butler–Volmer equation.^{24,25} Furthermore, Costentin and co-workers developed competing reaction-based pH-dependent models for homogeneous PCET reactions with water as the proton donor or acceptor.¹² Their work discussed various cases, such as the competition between concerted pathways with proton transfer within a local water cluster or directly to bulk solvent, the competition between concerted and stepwise pathways, and reactions involving buffer.

In this paper, we introduce a general, multichannel kinetic model to describe the pH dependence of homogeneous and heterogeneous PCET. This model yields a general expression for the pH-dependent apparent rate constants of both homogeneous PCET in solution and electrochemical PCET. The core concept of this model is that several ET and PCET channels are accessible and actively contribute to the overall PCET process. The contribution of each channel is strongly influenced by the relative populations of the different forms of the redox species (i.e., protonated or deprotonated and various hydrogen-bonded complexes with the proton donor or acceptor). These populations, described by the mole fractions, are pH-dependent and therefore lead to a complex dependence of the apparent rate constants on pH. Furthermore, we employ this model to describe experimentally measured pH-dependent kinetic data for a representative interfacial electrochemical PCET reaction, namely, reduction of a Ru-based water oxidation catalyst attached to a tin-doped In₂O₃ (ITO) surface.¹⁹ Our model explains the origins of the previously observed weak pH dependence of PCET for this system using physically meaningful parameters. Moreover, our model's predicted behavior for a wider pH range is then confirmed by additional experiments. This example highlights the importance of considering all possible reaction channels instead of just the dominant channel when analyzing experimental PCET kinetic data. Although this application focuses on electrochemical PCET, a future study will focus on applications of this kinetic model to homogeneous PCET systems.

THEORY

We use the four-channel model shown in Figure 1 as a typical example. Derivations for the general cases are provided in the Supporting Information. In our model, both the oxidized and reduced species can exist in protonated and deprotonated forms: Ox, OxH⁺, Red[−], and RedH. These species can be converted to each other via electron transfer (ET) and proton transfer (PT) to or from an external source. The edges of the square diagram in Figure 1 represent sequential ETPT or PTET pathways, and the diagonals of this diagram represent the concerted electron–proton transfer (EPT) pathways.^{26–29} Herein, the term PCET encompasses both sequential and concerted mechanisms, and the term EPT indicates concerted PCET. Assuming that buffer ions do not participate in the concerted pathways, either a hydronium ion H₃O⁺ or a water molecule can serve as the proton donor for the reduction reaction, and either a water molecule or a hydroxide ion OH[−] can serve as the proton acceptor for the oxidation reaction. If H₃O⁺ or OH[−] is the proton donor or acceptor in the concerted mechanism, the redox species must first form a hydrogen-bonded complex with the ion. These hydrogen-bonded complexes are denoted as {Ox⋯H₃O⁺} and {RedH⋯OH[−]}. The formation of these complexes is shown with black double

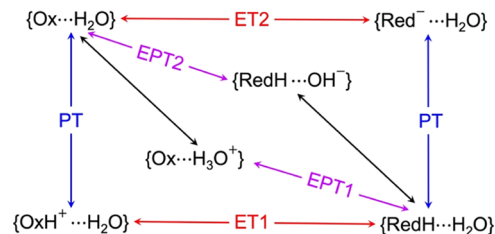
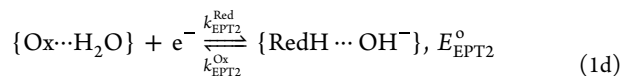
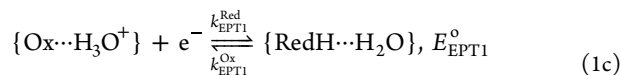
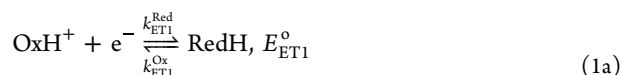


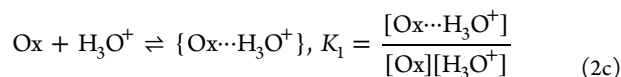
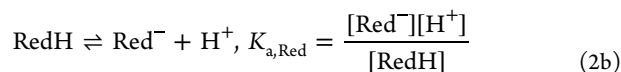
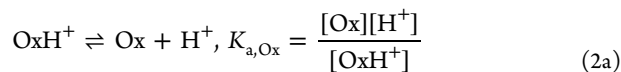
Figure 1. Schematic illustration of the four-channel model comprised of competing PCET reactions in aqueous solution. ET, PT, and EPT reactions are indicated by red, blue, and purple arrows, respectively. Hydrogen-bonded complex formation steps, which require interchange of water and H₃O⁺ or OH[−], are indicated by black arrows. Note that the ET and PT steps involve external electron and proton donors and acceptors that are not shown here. Starting at the top left, this diagram illustrates the four PCET channels: sequential PT–ET1, sequential ET2–PT, hydrogen-bonded complex formation followed by concerted EPT1, and concerted EPT2 followed by hydrogen-bonded complex dissociation.

arrows in Figure 1, requiring the displacement of a water molecule by either H₃O⁺ or OH[−]. On the other hand, if water is the proton donor or acceptor in the concerted mechanism, these additional hydrogen bond formation steps are not needed because the complexes with water are already formed upon solvation.

Next, we explicitly write the chemical reactions shown in Figure 1. For the remainder of this paper, we use the following convention. For ET, PT, and complex formation reactions, water is considered as a solvent, and the notation {X⋯H₂O} is dropped. For concerted EPT reactions, the notation {X⋯H₂O} must be written explicitly to ensure mass conservation. The ET and EPT channels (half reactions) are characterized by their standard potentials and rate constants, as given by the following expressions



Here, we consider a scenario in which the PT and complex formation steps are at equilibrium and are characterized by the corresponding equilibrium constants



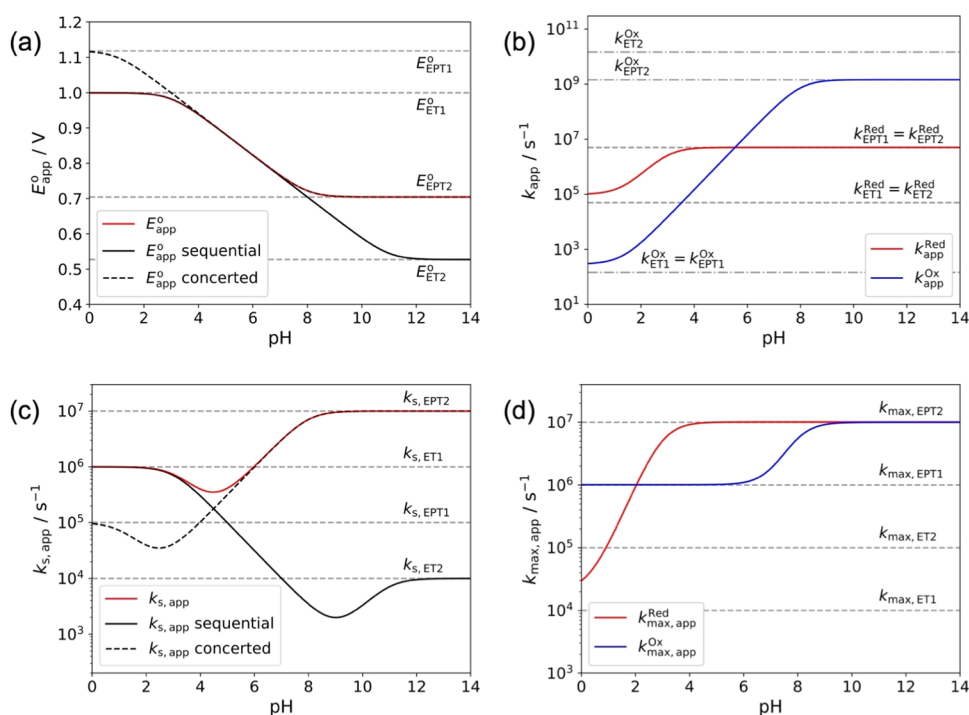
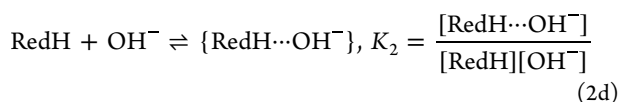
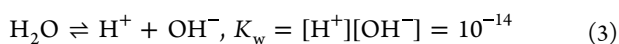


Figure 2. Representative illustrations of (a) E_{app}^0 , (b) k_{app} for electrochemical reactions at a specific potential, (c) $k_{s,app}$ for electrochemical reactions with the Butler–Volmer (BV) model, and (d) $k_{max,app}$ for electrochemical reactions with the Marcus–Gerischer (MG) model as functions of pH. These data were generated with the model described in Figure 1 and the associated equations given in the text. In these plots, $pK_{a,Ox} = 3$, $pK_{a,Red} = 11$, $pK_1 = -1$, and $pK_2 = -6$. The standard potential (vs NHE) of each channel is $E_{ET1}^0 = 1.00$ V, $E_{ET2}^0 = 0.53$ V, $E_{EPT1}^0 = 1.12$ V, and $E_{EPT2}^0 = 0.70$ V. Other parameters used for each plot are given in Table S1.



Equations 2a and 2b describe PT steps, corresponding to the blue arrows in Figure 1. Equations 2c and 2d describe the hydrogen-bonded complex formation steps, corresponding to the black arrows in Figure 1. In aqueous solution, we also consider the water dissociation equilibrium³⁰



This scenario, which is based on the equilibrium assumptions, is valid when PT and complex formation reactions are much faster than ET and EPT or when ET and EPT are photoinduced after sufficient mixing of the reactants.^{17,18}

The ET and EPT channels in Figure 1 can occur either electrochemically at an electrode surface or homogeneously with an external molecular reductant or oxidant. The following derivation will focus on electrochemical PCET, but the same equations have been adapted for homogeneous PCET (see the SI).

For the half-reaction $\text{Ox} + e^- \rightleftharpoons \text{Red}^-$, the concentrations of the oxidized and reduced species at the standard potential E^0 are equal: $[\text{Ox}] = [\text{Red}^-]$.³¹ Here, we neglect the difference between activities and concentrations and avoid introduction of the formal potential. For more complicated systems such as the four-channel model shown in Figure 1, each redox species can exist in different forms. In this case, we can define the apparent standard potential E_{app}^0 for each channel as the potential when the total concentrations of the oxidized and reduced species are equal: $[\text{Ox}_{tot}] = [\text{Red}_{tot}]$. In the general case, for the i th channel, $E_{app,i}^0$ can be calculated from the corresponding standard potential via the Nernst equation

$$E_{app,i}^0 = E_i^0 - \frac{RT}{F} \ln \frac{\chi_{\text{Red}_i}}{\chi_{\text{Ox}_i}} \quad (4)$$

where R is the universal gas constant, T is the temperature, and F is the Faraday constant. Here, χ_{Ox_i} and χ_{Red_i} are the mole fractions of Ox_i and Red_i , respectively, which are defined as the ratios between the concentration of the i th form and the total concentration

$$\chi_{\text{Ox}_i} = \frac{[\text{Ox}_i]}{[\text{Ox}_{tot}]} = \frac{[\text{Ox}_i]}{\sum_j [\text{Ox}_j]} \quad (5a)$$

$$\chi_{\text{Red}_i} = \frac{[\text{Red}_i]}{[\text{Red}_{tot}]} = \frac{[\text{Red}_i]}{\sum_j [\text{Red}_j]} \quad (5b)$$

Under the equilibrium assumption for the PT and complex formation steps, we can explicitly express χ_{Ox_i} and χ_{Red_i} for each form as a function of pH using the corresponding equilibrium constants (i.e., $K_{a,Ox}$, $K_{a,Red}$, K_1 , K_2 , and K_w in this example) as parameters. Moreover, the reactions in Figure 1 form a complete thermodynamic cycle, and therefore the standard potentials E_i^0 are related to each other through the same equilibrium constants. Under the equilibrium approximation, we can show that for any two channels i, j

$$E_{app,i}^0 = E_{app,j}^0, \forall i, j \quad (6)$$

Thus, for a multichannel PCET reaction system such as the one in Figure 1, there will be only one unique apparent potential. The full derivations and expressions associated with eqs 4–6 are provided in the Supporting Information.

Figure 2a shows the plot of E_{app}^0 as a function of pH. The red curve is calculated using eq 4, while the black solid and dashed

curves show the cases of including only the sequential or only the concerted pathways in Figure 1. For all three cases, the curve has the expected shape. For the sequential-only case, when $\text{pH} < \text{p}K_{\text{a,ox}}$, $E_{\text{app}}^{\circ} = E_{\text{ET1}}^{\circ}$; at intermediate pH, E_{app}° decreases linearly as pH increases with a slope of 59 mV per pH unit; when $\text{pH} > \text{p}K_{\text{a,red}}$, $E_{\text{app}}^{\circ} = E_{\text{ET2}}^{\circ}$. For the concerted-only case, E_{app}° has the same behavior, but the upper and lower bounds become E_{EPT1}° and E_{EPT2}° , and the transition points become $-\text{p}K_1$ and $\text{p}K_2 + \text{p}K_w$, respectively. The slope at intermediate pH is still 59 mV per pH unit. When both mechanisms are considered, the resulting curve can be seen as connecting pieces of the two black curves. The plateau value at low pH is the lower potential of E_{ET1}° versus E_{EPT1}° with a turning point at the larger value of $-\text{p}K_1$ versus $\text{p}K_{\text{a,ox}}$. The plateau value at high pH is the higher potential of E_{ET2}° versus E_{EPT2}° with a turning point at the lower value of $\text{p}K_2 + \text{p}K_w$ versus $\text{p}K_{\text{a,red}}$.

Next, we move on to the derivation of the apparent rate constants. Here, we assume that each form of the reduced or oxidized species is not distinguished in kinetics experiments, and only the total reduction or oxidation rate is measured. Although some forms may be distinguishable because they have distinct spectra, formulating the equations in this manner provides a general approach for kinetic analysis.

For an electrochemical reaction, ET occurs between the main redox species undergoing PCET and the electrode. In this case, the total reduction and oxidation rates of all forms of the redox species are

$$r_{\text{Red}}(E) = \sum_i k_i^{\text{Red}}(E)[\text{Ox}_i] \quad (7a)$$

$$r_{\text{Ox}}(E) = \sum_i k_i^{\text{Ox}}(E)[\text{Red}_i] \quad (7b)$$

where $k_i^{\text{Red}}(E)$ and $k_i^{\text{Ox}}(E)$ are the reduction and oxidation rate constants of the i th channel and E is the electrode potential. These rate constants are potential-dependent and are related to each other via the reaction free energy $\Delta G_i = F(E - E_i^{\circ})$

$$\ln \frac{k_i^{\text{Red}}(E)}{k_i^{\text{Ox}}(E)} = -\frac{F(E - E_i^{\circ})}{RT} \quad (8)$$

These total reaction rates can be written as the product of an apparent rate constant, $k_{\text{app}}^{\text{Red}}$ or $k_{\text{app}}^{\text{Ox}}$, and the total concentration of the redox species $[\text{Ox}_{\text{tot}}]$ or $[\text{Red}_{\text{tot}}]$. The resulting apparent rate constants are the weighted averages of the rate constants of each redox channel, where the weights are the mole fractions of the corresponding reactants

$$k_{\text{app}}^{\text{Red}}(E) = \sum_i k_i^{\text{Red}}(E)\chi_{\text{Ox}_i} \quad (9a)$$

$$k_{\text{app}}^{\text{Ox}}(E) = \sum_i k_i^{\text{Ox}}(E)\chi_{\text{Red}_i} \quad (9b)$$

Given these expressions, it can be shown that

$$\ln \frac{k_{\text{app}}^{\text{Red}}(E)}{k_{\text{app}}^{\text{Ox}}(E)} = -\frac{F(E - E_{\text{app}}^{\circ})}{RT} \quad (10)$$

Equations 9a, 9b, and 10 hold for any kinetic models describing $k_i^{\text{Red}}(E)$ and $k_i^{\text{Ox}}(E)$, including the widely used Butler–Volmer (BV)^{24,25} and Marcus–Gerischer (MG)^{24,32–35} models. Although both the BV and MG models

were originally derived for ET reactions, they can be extended to concerted PCET reactions. The BV model assumes a linear free energy relationship, where the ET free energy barrier is proportional to the ET driving force,²⁴ and can be generalized to concerted PCET reactions by replacing the redox potential with the proton-coupled redox potential in the expressions. Moreover, we have shown that the MG theory can be extended to describe concerted PCET reactions within the framework of our vibronically nonadiabatic PCET theory^{19,36} by including the transitions between all reactant and product vibronic states. Figure 2b shows the potential-dependent $k_{\text{app}}^{\text{Red}}$ and $k_{\text{app}}^{\text{Ox}}$ as functions of pH at a given electrode potential. The oxidation apparent rate constant has a slope of $\frac{d \log k}{d \text{pH}} = 1$, whereas the reduction apparent rate constant has a slope of 0.63, which is less than unity, indicating that the reduction reaction has a weaker pH dependence. In general, both reduction and oxidation reactions can exhibit weak pH dependence in this model. A detailed analysis of this figure is provided in the SI.

There are also multiple ways to define a potential-independent rate constant. The standard rate constant k_s is defined as the rate constant when $E = E^{\circ}$.^{24,25} At this potential, the reaction free energy $\Delta G = F(E - E^{\circ}) = 0$ so $k^{\text{Red}} = k^{\text{Ox}} \equiv k_s$. Alternatively, if the reaction rate constant saturates at very negative or positive potentials, maximum rate constants k_{max} for reduction and oxidation can be defined at $E \rightarrow \pm \infty$.^{24,32–35} Similarly, we can define the potential-independent apparent standard rate constant and apparent maximum rate constants as

$$k_{s,\text{app}} = k_{\text{app}}^{\text{Red}}(E_{\text{app}}^{\circ}) = k_{\text{app}}^{\text{Ox}}(E_{\text{app}}^{\circ}) \quad (11a)$$

$$k_{\text{max},\text{app}}^{\text{Red}} = k_{\text{app}}^{\text{Red}}(E \rightarrow -\infty) \quad (11b)$$

$$k_{\text{max},\text{app}}^{\text{Ox}} = k_{\text{app}}^{\text{Ox}}(E \rightarrow +\infty) \quad (11c)$$

Here, E_{app}° is the apparent standard potential defined in eq 4. In practice, $k_{\text{max},\text{app}}$ can also be defined at the experimental potential limits. The apparent standard or maximum rate constants can then be obtained by substituting the expressions for $k_i^{\text{Red}}(E)$ and $k_i^{\text{Ox}}(E)$ into Equations 9a and 9b and setting $E = E_{\text{app}}^{\circ}$ or $\pm \infty$. The general expressions for $k_{s,\text{app}}$ and $k_{\text{max},\text{app}}^{\text{Red/Ox}}$ are provided in the Supporting Information. For the BV and MG kinetic models, the results are presented in Table 1. Representative illustrations of these cases are shown in Figure 2c,d, and detailed analyses are provided in the SI.

To conclude this section, we summarize the expressions for the apparent rate constants for both homogeneous and electrochemical PCET reactions in Table 1. Note that these equations are not limited to the four-channel case shown in Figure 1. Certain channels can be shut down by excluding the corresponding form of Ox_i and Red_i or setting certain $k_i = 0$. For example, if we exclude all concerted pathways in Figure 1 and apply the equation for BV kinetics $k_{s,\text{app}}^{\text{BV}}$, this model is reduced to Laviron's model, and we obtain the same expression for the apparent standard rate constant (see the SI). More generally, other channels could be added, such as concerted pathways with buffer as the proton donor or acceptor, and the assumption of equilibrium for PT and complex formation could be removed, leading to more complex kinetic equations.

Table 1. Summary of the Expressions for Apparent Rate Constants of Homogeneous and Electrochemical PCET Reactions

system	type of kinetics	apparent rate constant
homogeneous	NA	$k_{\text{app}}^{\text{Red}} = \sum_i k_i^{\text{Red}} \chi_{\text{Ox}_i}$ $k_{\text{app}}^{\text{Ox}} = \sum_i k_i^{\text{Ox}} \chi_{\text{Red}_i}$
electrochemical (potential-dependent rate constant)	general	$k_{\text{app}}^{\text{Red}}(E) = \sum_i k_i^{\text{Red}}(E) \chi_{\text{Ox}_i}$ $k_{\text{app}}^{\text{Ox}}(E) = \sum_i k_i^{\text{Ox}}(E) \chi_{\text{Red}_i}$
electrochemical (potential-independent rate constant)	Butler–Volmer ^a	$k_{\text{s,app}}^{\text{BV}} = \sum_i k_{\text{s},i} (\chi_{\text{Ox}_i})^{1-\alpha_i} (\chi_{\text{Red}_i})^{\alpha_i}$
	Marcus–Gerischer ^b	$k_{\text{max,app}}^{\text{MG,Red}} = \sum_i k_{\text{max},i} \chi_{\text{Ox}_i}$ $k_{\text{max,app}}^{\text{MG,Ox}} = \sum_i k_{\text{max},i} \chi_{\text{Red}_i}$

^a α_i and $k_{\text{s},i}$ are the cathodic transfer coefficient and the standard rate constant for the i th channel, respectively. ^b $k_{\text{max},i}$ is the maximum rate constant for the i th channel.

RESULTS AND DISCUSSION

We applied our model to an electrochemical PCET reaction, namely, PCET to a Ru-based water oxidation catalyst^{37–44} attached to an ITO surface. As discussed above, the apparent rate constant of an electrochemical PCET reaction is not only pH-dependent but also potential-dependent. Kessinger et al. studied the interfacial ET and PCET reactions in a Ru-based water oxidation catalyst, $[\text{Ru}^{\text{II}}(\text{tpy})(\text{bpy})(\text{H}_2\text{O})]^{2+}$, $\text{Ru}^{\text{II}}-\text{OH}_2$, (tpy = 2,2':6',2''-terpyridine, bpy = 2,2'-bipyridine), attached to ITO.¹⁹ Photoexcitation of $\text{Ru}^{\text{II}}-\text{OH}_2$ results in rapid electron transfer to the ITO electrode, producing $\text{Ru}^{\text{III}}-\text{OH}_2/\text{OH}^-$ with a protonation state that is dependent on the solution pH. The resulting back electron transfer reaction from ITO to $\text{Ru}^{\text{III}}-\text{OH}_2/\text{OH}^-$ that regenerates $\text{Ru}^{\text{II}}-\text{OH}_2$ therefore occurs via an ET and/or a PCET pathway. This reduction reaction was monitored using transient absorption spectroscopy by measuring the recovery of the metal-to-ligand charge-transfer (MLCT) absorption peak of $\text{Ru}^{\text{II}}-\text{OH}_2$.

The apparent reduction rate constants $k_{\text{app}}^{\text{Red}}$ were measured at pH = 1, 3, and 5 at various applied potentials, thereby altering the driving force $-\Delta G^\circ$. The potential-dependent apparent rate constant of this interfacial ET/PCET system can be described by the MG theory, where the rate constant plateaus at a large driving force. Based on the experimentally measured $\text{p}K_{\text{a}}$ of the $\text{Ru}^{\text{III}}-\text{OH}_2$ complex attached to ITO, the mechanism was presumed to be ET at pH = 1 but PCET at pH = 3 and 5. At low pH, the axial ligand coordinated to Ru is H_2O , and therefore only ET is possible, but at higher pH, the ligand coordinated to Ru is OH^- , and ET is accompanied by proton transfer to the OH^- ligand to generate a water ligand. A weak pH dependence was observed for the overall process. When the pH increases from 3 to 5, the maximum rate constant only decreases by around 3-fold rather than decreasing 100-fold, as would be expected according to a model based on a single PCET pathway with H_3O^+ as the proton donor, or being pH-independent, as would be expected according to a model based on a single PCET pathway with H_2O as the proton donor.¹⁹

Here, we focus on the PCET process associated with the reduction of the Ru^{III} catalyst^{37–44} attached to ITO. The two ET and two EPT channels, as well as Ox, OxH^+ , Red^- , and RedH for this process, are depicted in Figure 3. As no buffer solution was added in the experiments,¹⁹ the diagram in Figure 1 gives a complete set of the possible ET and EPT channels in this system, which is recreated using system-specific notation in Figure 4. The experimental rate constant was obtained by analyzing the absorbance change of the Ru^{II} catalyst (the product) as a function of time. In this system, the Ru^{III} catalyst, which is the reactant, is generated by photoexcitation. The equilibrium assumption thus requires PT and complex association to be faster than ET and EPT. This assumption is reasonable for this system in the pH and potential range studied experimentally (see the SI). Note that the experimental measurement of the change in total concentration of the reduced species (i.e., the Ru^{II} catalyst) is consistent with our

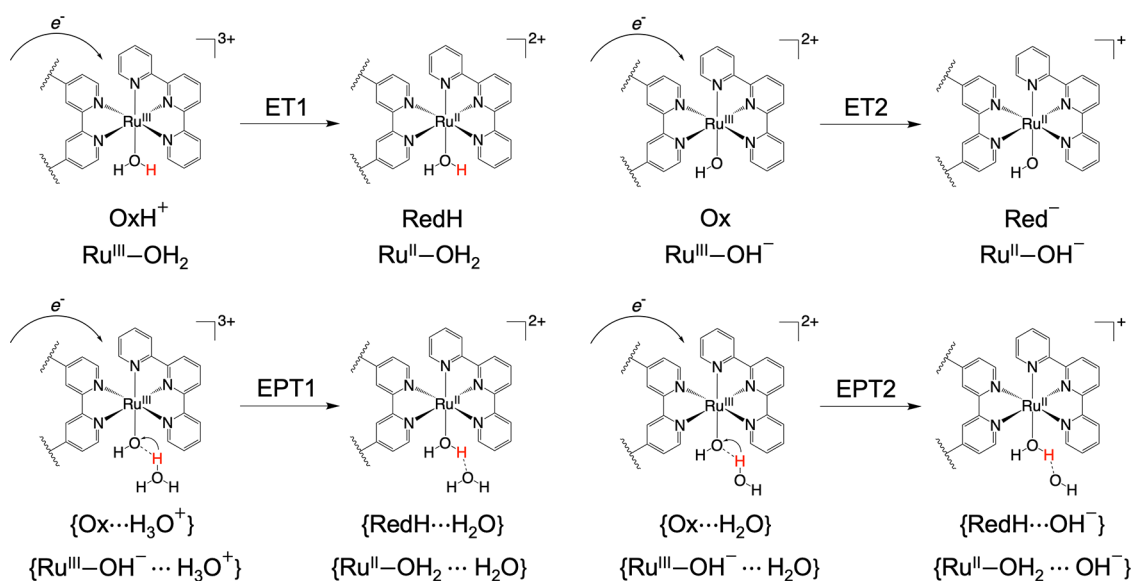


Figure 3. Reaction mechanisms of the two ET and two EPT channels for the water oxidation catalyst undergoing electrochemical PCET. Schematic structures of Ox, OxH^+ , Red^- , RedH , and the associated complexes are labeled. The transferring proton is colored red. The charge given for each species includes the H_3O^+ and OH^- charges, which are therefore not shown explicitly.

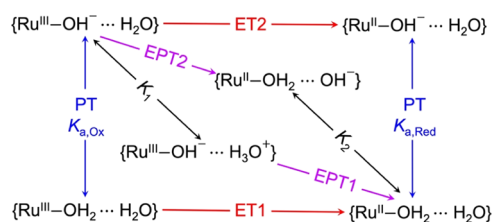


Figure 4. Schematic illustration of the four-channel model for the ITO-Ru system. The system-specific notation defined in Figure 3 is used. ET and EPT reactions are indicated by red and purple single-headed arrows, respectively, in the direction corresponding to reduction. The equilibrium constants $K_{a,Ox}$, $K_{a,Red}$, K_1 , and K_2 , corresponding to PT and hydrogen-bonded complex formation/dissociation steps, are indicated by blue and black double-headed arrows, respectively.

kinetic model, which tracks the total concentrations of the reduced and oxidized species.

Prior to analyzing the experimental data, we introduce certain physically motivated assumptions regarding the parameters. We can estimate the values of K_1 and K_2 using density functional theory (DFT) calculations in conjunction with the experimentally measured $pK_{a,Ox}$ and $pK_{a,Red}$. These calculations lead to estimates of $K_1 \approx 10^{0.2}$ and $K_2 < 10^{4.5}$ (see the SI). Furthermore, since the potential-dependent rate constant can be well described by MG theory, the maximum rate constant has the same expression for both ET and EPT¹⁹

$$k_{\max} = \frac{2\pi}{\hbar} \rho(\epsilon_F) |V_{el}|^2 \quad (12)$$

where $\rho(\epsilon_F)$ is the density of states at the Fermi level of the electrode and V_{el} is the electronic coupling between the electrode and the redox molecule. For a surface-attached molecule, it is reasonable to assume that the electronic coupling is approximately the same if the ligands are the same for the reactant species. Therefore, we will assume that $k_{\max,ET2} = k_{\max,EPT1} = k_{\max,EPT2}$ because the ligand is OH^- for the reactant in each of the three channels (Figure 3).

For electrochemical systems, the apparent pK_a of a surface-attached molecule has been reported to depend on an applied potential.⁴⁵ When the potential becomes more negative, the negative charge accumulating on the electrode surface will disfavor deprotonation of the attached catalyst. This potential-

dependent behavior has been observed in experiments on metal surfaces and described in terms of an increase of ~ 0.10 pK_a unit per 59 mV of potential decrease.⁴⁵ ITO, a degenerate semiconductor, is expected to exhibit similar behavior due to its metal-like conductivity and carrier density ($\sim 10^{20}$ cm^{-3}).^{24,46,47} For the ITO-Ru system, the $pK_{a,Ox}$ is measured to be 1.2 at 1.1 V vs NHE, and the apparent rate constant reaches its maximum value in the range of -0.1 to $+0.1$ V vs NHE for pH of 1, 3, or 5 (symbols in Figure 5a).¹⁹ To reproduce the experimental data with our model, we used a slope of $a = 0.12$ pK_a unit per 59 mV of potential decrease, similar to previous findings.⁴⁵ Thus, the potential dependence of $pK_{a,Ox}$ was modeled as

$$pK_{a,Ox}(E) = -0.12 \times \frac{E - 1.1 \text{ V}}{0.059 \text{ V}} + 1.2 \quad (13)$$

Note that this potential dependence on ITO has not been experimentally verified. Anchoring a Ru^{II} water oxidation catalyst with a pH-sensitive visible absorption spectrum⁴⁸ to the surface and monitoring its spectral behavior with an applied potential could provide useful insights. We also investigated models where $pK_{a,Ox}$ is independent of the potential E and found that such models could only reproduce the experimental data at higher pH, such as pH = 5, but not for the entire pH range (Figure S5). For the ITO-Ru system, $pK_{a,Red}$ cannot be measured for the attached complex due to the instability of the phosphonate anchoring group at pH > 5.⁴⁹ We also used eq 13 to describe the potential dependence of $pK_{a,Red}$ with a value of 8.2 at 1.1 V, which will give a value of ~ 9.2 at E_{ET2}^0 to be consistent with the Pourbaix diagram of the free complex in solution. We found that the results using a higher value could not reproduce the results at pH = 5.

This potential-dependent apparent pK_a of the surface-attached species can also be viewed in terms of a potential-dependent work term due to bringing a proton to the interfacial region. A similar work term is necessary for the ET steps for the same physical reason and to ensure that the overall free energy of the PCET process is independent of path. Therefore, this work term was added to all of the ET and PT steps. Including these work terms for the diagonal steps does not alter the results because they effectively cancel. These work terms are effectively accounting for nonideal behavior at the interface.^{50,51} The impact of the potential dependence of

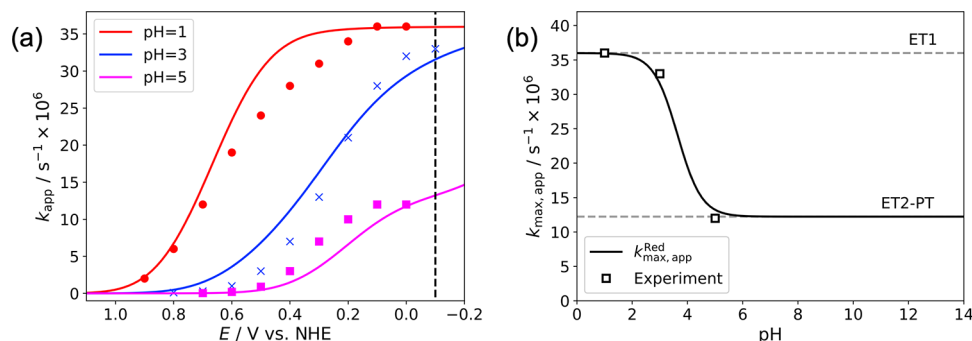


Figure 5. (a) Modeled potential-dependent apparent PCET rate constant for reduction of Ru^{III} complex attached to ITO surface at pH = 1, 3, and 5. The dots, crosses, and squares are the experimental data at different pH obtained from ref 19, and the solid lines were produced by our model using the parameters provided in the SI. (b) Modeled apparent maximum PCET rate constant $k_{\max,app}$ as a function of pH. $k_{\max,app}$ is calculated at $E = -0.1$ V vs NHE, shown as the black dashed line in panel (a). The open square are experimental data from ref 19. The superscript MG is dropped in this figure to simplify the notation. The dominant channels at low and high pH values are annotated in panel (b). The parameters used for this figure are given in Table S2.

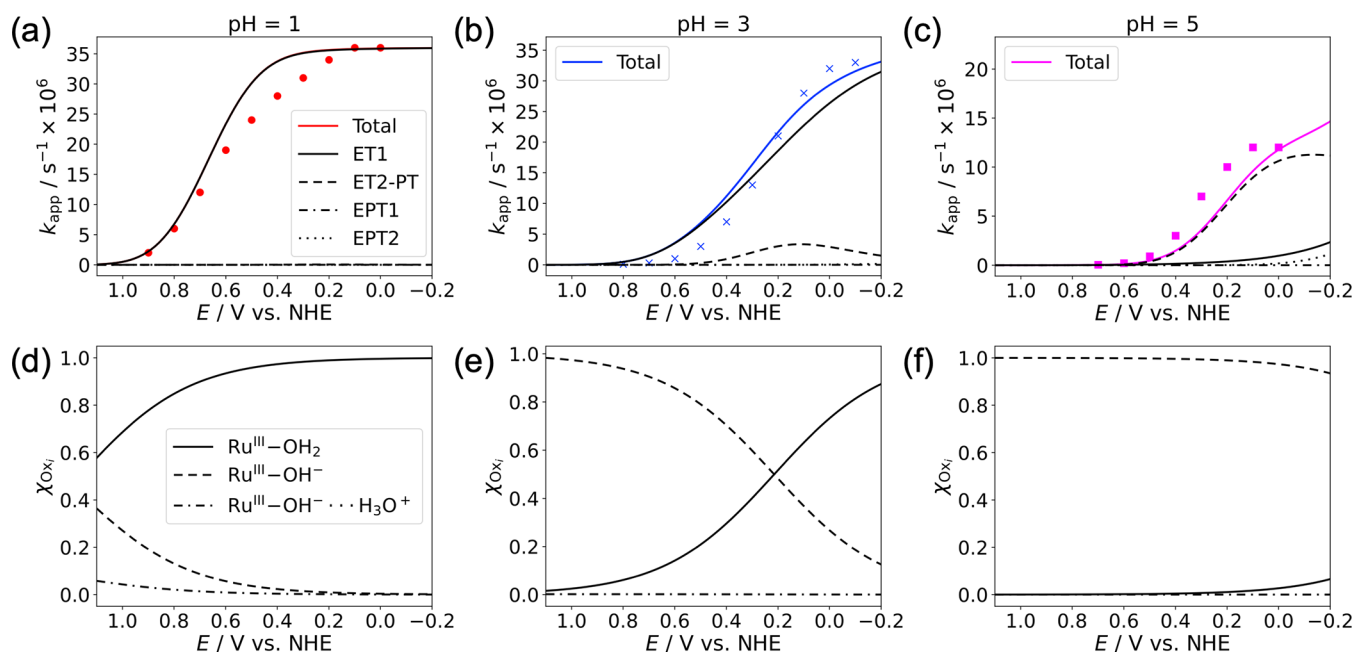


Figure 6. (a–c) Contributions of each channel to the total rate constant at (a) pH = 1, (b) pH = 3, and (c) pH = 5. The definitions of the individual channels are given in Figure 3. The symbols are experimental data. (d–f) Mole fraction of each form at (d) pH = 1, (e) pH = 3, and (f) pH = 5. Note that the forms of the oxidized species in panels (d–f) correspond to the reactants for the channels of the same line types in panels (a–c). The $Ru^{III}-OH^-$ form encompasses the reactants of both ET2 and EPT2. The standard potential (vs NHE) of each channel is $E_{ET1}^0 = 1.10$ V, $E_{ET2}^0 = 0.63$ V, $E_{EPT1}^0 = 1.16$ V, and $E_{EPT2}^0 = 0.52$ V. Other parameters used for this figure are given in Table S2.

the apparent pK_a values on the pH dependence of the apparent potential is negligible (Figure S9) and is not expected to be experimentally observable for this system.

Within the MG theory, the potential-dependent apparent rate constant can be expressed as

$$k^{MG,Red}(E) = k_{max} \cdot \frac{1}{2} \left[1 - \operatorname{erf} \left(\frac{F(E - E^0) + \lambda}{2\sqrt{\lambda RT}} \right) \right] \quad (14)$$

where λ is the reorganization energy. The apparent reorganization energy can be defined as the driving force corresponding to the potential at which this rate constant reaches half its maximum value (i.e., $k^{MG,Red}(E)/k_{max} = 1/2$ when $F(E^0 - E) = \lambda$). Using the rate constant expression of the MG theory, Equation 9a becomes

$$k_{app}^{MG,Red}(E, pH) = \sum_i k_{max,i} \cdot \frac{1}{2} \left[1 - \operatorname{erf} \left(\frac{F(E - E_i^0) + \lambda_i}{2\sqrt{\lambda_i RT}} \right) \right] \chi_{Ox_i}(pH; pK_{a,Ox}(E)) \quad (15)$$

We estimated the total reorganization energies for ET and EPT to be 0.37 and 1.01 eV, respectively, based on our previous calculations.¹⁹ In this previous work, the outer-sphere (solvent) reorganization energy was computed using a dielectric continuum model with a cylindrical cavity containing a point charge representing the molecular catalyst, as well as the bridge attaching it to the electrode surface (Figure S10). The resulting outer-sphere reorganization energy was computed to be 0.21 eV and was assumed to be the same for ET and EPT. In this previous work, the inner-sphere (solute) reorganization energies were computed using the four-

point method for ET⁵² and the modified four-point method for EPT.⁵³ Geometry optimizations of the oxidized and reduced forms of the molecular catalyst and single-point energy calculations of each geometry in the alternative redox state, as well as optimization of the proton position for EPT, were performed using DFT. For ET, the axial ligand is H_2O in the oxidized and reduced states, whereas for EPT, the axial ligand is OH^- in the oxidized state and H_2O in the reduced state. The inner-sphere reorganization energies were computed to be 0.16 and 0.54 eV for ET and EPT, respectively. The substantial difference arises from the larger change in the distance between Ru and the oxygen of the axial ligand for EPT than for ET (0.19 Å for EPT versus 0.06 Å for ET). The total reorganization energy, which is the sum of the inner- and outer-sphere components, computed for ET is in agreement with experimental measurements at low pH, where only the ET channel is accessible.¹⁹ The total reorganization energy for EPT is an effective value where the contributions of excited proton vibrational states are also included. A model using λ_{EPT} without considering the excited proton vibrational states is provided in the SI (Figure S7).

Using the parameter values provided and explained in Table S2, we are able to model the pH and potential dependence of the apparent PCET rate constant, as shown in Figure 5. Figure 5a shows qualitatively reasonable agreement with the experimental data in this potential and pH range using eq 15. The weak pH dependence of $k_{max,app}$ is correctly described, and the curves for pH = 3 and 5 are shifted toward lower potentials compared to the curve for pH = 1, indicating larger apparent reorganization energies for pH = 3 and 5. Note that this apparent reorganization energy reflects the summation over channels in eq 15 and thus is not as easily interpreted as in eq 14, as discussed further below. One source of the quantitative deviations could be the use of the error function expression in eq 15. In this expression, we assume that the

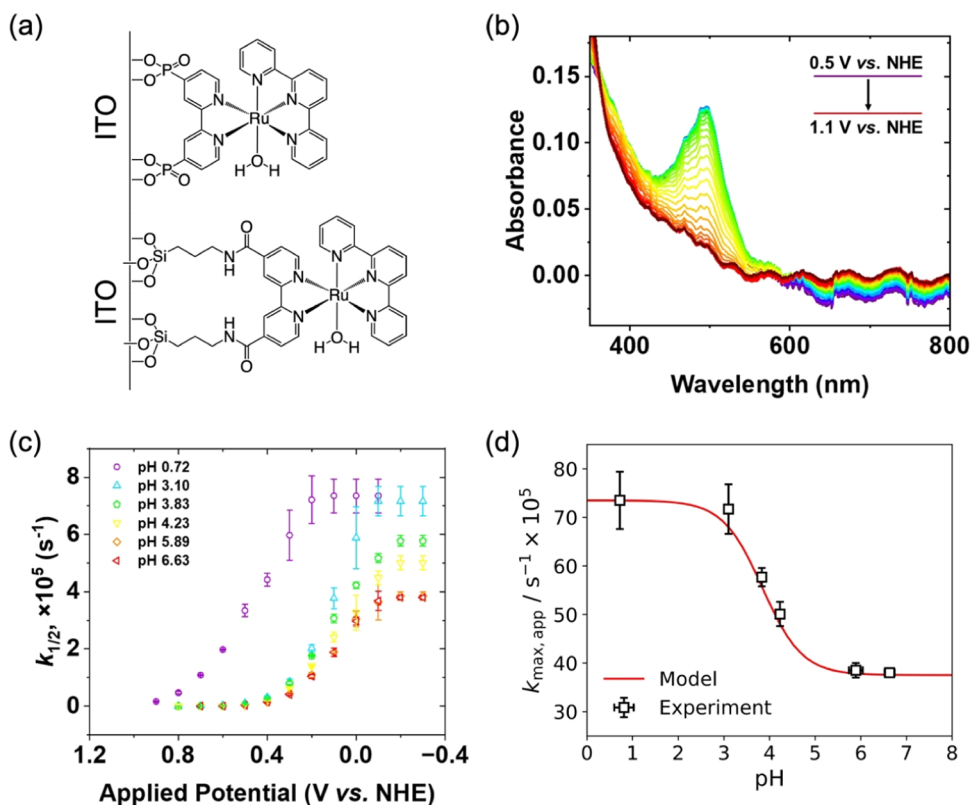


Figure 7. (a) Structures of the catalyst when anchored to a metal oxide electrode through either phosphonate (top) or siloxane (bottom) anchor groups. (b) Spectroelectrochemistry of the catalyst upon the addition of a positive applied potential from 0.5 V vs NHE to 1.1 V vs NHE. (c) Pseudo-rate constant ($k_{1/2}$) as a function of applied potential for the reaction between electrons in ITO and the oxidized catalyst at the indicated pH values. (d) Maximum rate constant $k_{\max,app}$ as a function of the solution pH. The y-error bars represent one standard deviation from the average of three separate electrode measurements, while the x-error bars represent one standard deviation from the average pH recorded for the electrolyte solution both before and after the experiment for each of the three trials. The red curve was generated with the kinetic model using the parameters given in Table S3.

density of states of the electrode is constant, and the electronic coupling is the same for all electrode energy levels, but these assumptions may not be rigorously valid for real systems. On the other hand, the agreement with the experimental data at pH = 1 can be significantly improved if we adjust K_1 (Figure S6). Moreover, the slight increase of the pH = 5 curve in Figure 5a at around -0.2 V vs NHE does not appear when a larger λ_{EPT} is used (Figure S8). Figure 5b shows the apparent maximum rate constant as a function of pH. Here, the apparent maximum rate constant is defined at the lowest potential reached in the experiment, $E = -0.1$ V, instead of $E = -\infty$, because not all channels reach saturation in the experimental potential range. Using the same parameters as in Figure 5a, we predict that the apparent maximum PCET rate constant will become pH-independent at high pH. This prediction is confirmed by experimental measurements, as discussed below.

To understand the origin of the weak pH dependence of $k_{\max,app}$, we analyzed the contributions of each channel at pH = 1, 3, and 5 as a function of potential (Figure 6a–c). With the equilibrium assumption, when $\text{pH} < \text{p}K_{a,\text{Red}}$ any $\text{Ru}^{\text{II}}-\text{OH}^-$ (Red $^-$) formed through ET2 will nearly instantaneously be protonated to form $\text{Ru}^{\text{II}}-\text{OH}_2$ (RedH). Therefore, ET2 is a PCET channel occurring by the ETPT mechanism. In principle, ET1 is associated with a PCET channel occurring by the PTET mechanism, where the protonation occurs via a pre-equilibrium process. The contribution of each channel to the total rate constant is determined by both the mole fractions

of the reactant forms χ_{Ox_i} (Figure 6d–f) and their corresponding rate constants. For this system, our previous work showed that the total reorganization energy is significantly larger for EPT than for ET,¹⁹ as discussed above, leading to a higher free energy barrier for the EPT steps. As a result, the ET rate constants are significantly larger than the EPT rate constants at a given electrode potential. Moreover, at a given potential, ET1 is faster than ET2 because it has a more positive reduction potential (i.e., a larger driving force).

At pH = 1, the ET1 channel dominates over the entire range of potentials considered (Figure 6a). The concentration of $\text{Ru}^{\text{III}}-\text{OH}^-$ (Ox) is much smaller than $\text{Ru}^{\text{III}}-\text{OH}_2$ (OxH $^+$) over this potential range because the potential-dependent $\text{p}K_{a,\text{Ox}}$ is always greater than the pH. Therefore, the ET2, EPT1, and EPT2 channels are not accessible due to the low concentration of Ox, especially at negative potentials. Thus, the ET1 channel dominates at pH = 1.

At pH = 3, the ET1 channel still dominates, although the ET2-PT channel also contributes to a smaller extent at less positive potentials. The concentration of $\text{Ru}^{\text{III}}-\text{OH}_2$ is negligible at 1.1 V vs NHE because $\text{p}K_{a,\text{Ox}} = 1.2$ at this potential, thereby inhibiting contributions from the ET1 channel at this potential. Assuming the potential dependence of $\text{p}K_{a,\text{Ox}}$ given in eq 13, however, the concentrations of $\text{Ru}^{\text{III}}-\text{OH}_2$ and $\text{Ru}^{\text{III}}-\text{OH}^-$ become comparable at less positive potentials (Figure 6e). Since ET1 is much faster than the other

channels for reasons discussed above, the ET1 channel dominates the reduction at pH = 3 (Figure 6b). The ET2-PT channel contributes in the region of potential at which $F(E - E_{\text{ET}2}^0) \approx -\lambda_{\text{ET}}$ due to the error function form of the rate constant in eq 14.

At pH = 5, the ET2-PT channel dominates over the entire range of potentials considered (Figure 6c). The concentration of $\text{Ru}^{\text{III}}-\text{OH}_2$ at this pH is much smaller, virtually eliminating the contribution from the ET1 channel. The EPT1 channel is also not accessible because the mole fraction of $\text{Ru}^{\text{III}}-\text{OH}^-\cdots\text{H}_3\text{O}^+$ ($\text{Ox}\cdots\text{H}_3\text{O}^+$) is negligible at this pH. Moreover, ET2 is much faster than EPT2 due to its smaller reorganization energy. For these reasons, the ET2-PT channel is dominant at pH = 5.

Thus, at pH = 1, 3, and 5, the two major competing channels are the ET1 and ET2 channels, corresponding to PCET via the PTET and ETPT mechanisms, respectively. Both the ET1 and ET2 rate constants are pH-independent. The ET1 channel dominates at pH = 1 and 3, whereas the ET2-PT channel dominates at pH = 5. This interpretation is supported by the experimentally measured maximum rate constants and corresponding electronic coupling H_{ab} , which are similar at pH = 1 and 3 but significantly different at pH = 5 (see Figure 5a, where the maximum value is similar for the red and blue curves but different for the magenta curve). This experimental observation is consistent with the same dominant channel at pH = 1 and 3 but a different dominant channel at pH = 5. The weak pH dependence observed experimentally arises from the intrinsic difference between the rate constants of the ET1 and ET2-PT channels due to their distinct electronic coupling and the change of their relative contributions with pH due to the changes in the mole fractions of $\text{Ru}^{\text{III}}-\text{OH}^-$ and $\text{Ru}^{\text{III}}-\text{OH}_2$.

This analysis also provides insights into the change of apparent reorganization energy at pH = 1, 3, and 5. The apparent reorganization energy is extracted as the driving force when $k_{\text{app}} = \frac{1}{2}k_{\text{max,app}}$. At pH = 3 and 5, the $k(E)$ curve is shifted toward lower potential compared to the curve at pH = 1, leading to larger apparent reorganization energies for pH = 3 and 5 compared to pH = 1. These observations could be interpreted to suggest the same mechanism at pH = 3 and 5 and a different mechanism at pH = 1. However, our general model suggests an alternative interpretation. The dominant channel is the same at pH = 1 and pH = 3, and the curve shift for pH = 3 leading to a higher apparent reorganization energy is due to the negligible mole fraction of $\text{Ru}^{\text{III}}-\text{OH}_2$ at high (positive) potentials and the increased mole fraction of $\text{Ru}^{\text{III}}-\text{OH}_2$ at lower potentials. At pH = 5, the ET2-PT channel dominates, and the difference in reduction potential for ET2 compared to ET1 leads to the curve shift. It is somewhat fortuitous that the apparent reorganization energy is nearly the same at pH = 3 and 5.

Finally, we designed new experiments to test the model prediction of $k_{\text{max,app}}$ at higher pH. Figure 7a shows the structures of the catalyst when anchored to a metal oxide electrode. In the previous study,¹⁹ phosphonate anchor groups (top) were used. These anchors are unstable at pH > 5, thus prohibiting electrochemical PCET kinetics measurement at higher pH. Here, we prepared a new Ru-based water catalyst with siloxane anchor groups (bottom in Figure 7a). Detailed synthetic procedures and characterizations are provided in the SI. The siloxane anchor is stable over a much wider pH range of 0.5–12, allowing us to quantify the pH dependence over the

entire pH range. Similar to the previously studied catalyst, when anchored on the ITO surface, this new Ru^{II} catalyst also has an MLCT absorption band centered around 495 nm. When a positive potential sufficient to oxidize the ruthenium center from Ru^{II} to Ru^{III} is applied to the film, this feature is attenuated, indicating oxidation of the ruthenium center (Figure 7b).

Using transient absorption spectroscopy and monitoring the recovery of the MLCT absorption of the Ru^{II} complex, the interfacial ET and PCET reaction kinetics were quantified from pH 0.7 to 6.8. The kinetics as a function of the applied potential for the reaction at each pH are provided in Figure 7c, and a plot of the maximum rate constant for the PCET reaction as a function of pH is shown in Figure 7d. For pH < 5, we observed the same behavior as in our previous study. The $k_{\text{app}}(E)$ curves for pH > 3 are shifted toward lower potentials compared to the curve for pH = 0.7. For the maximum rate constant, the value at pH = 3.10 is similar to that at pH = 0.7, and a weak decrease is observed in the pH range of 3–5. On the other hand, the $k_{\text{app}}(E)$ curves for pH = 6.63 is right on top of the curve at pH = 5.89, indicating pH independence in this pH range. The plot of $k_{\text{max,app}}$ also levels off when pH > 5. These experimental observations provide validation for our model prediction (Figure 5b) that the apparent maximum PCET rate constant will become pH-independent at higher pH.

CONCLUSIONS

In this paper, we developed a multichannel kinetic model to describe the pH dependence of PCET reactions. The apparent standard potential and apparent rate constant can be expressed as functions of the mole fractions of different forms of the reactant (i.e., the protonated and deprotonated forms), which in turn depend on pH. We derived the general expressions for the apparent rate constants of both homogeneous and electrochemical PCET reactions and the specific expressions corresponding to Butler–Volmer and Marcus–Gerischer kinetics. The power of this model is that the multiple competing channels encompass both sequential and concerted mechanisms and, in contrast to common square schemes, the possibility of more than one proton donor and acceptor.

We also applied this model to the light-initiated electrochemical reduction of an ITO-attached Ru-based water oxidation catalyst and explained the experimentally observed weak pH dependence of the maximum rate constant for pH between 1 and 5. Our analysis indicates that the hydronium ion is not directly involved in a concerted PCET reaction involving proton transfer from the hydronium to a hydroxide axial ligand upon reduction of the ruthenium center. Instead, our analysis suggests that the dominant channels are either ET, where the axial ligand is water, or PCET via an ETPT mechanism, where reduction of the ruthenium is followed quickly by protonation of the hydroxide axial ligand. At low pH, the dominant channel is ET, whereas at higher pH, the mechanism becomes PCET via the ETPT mechanism. The observed pH dependence arises from the intrinsic difference between the rate constants of these two channels and the dependence of their relative contributions, as determined by the reactant mole fractions, on pH. Our model also predicts that the maximum rate constant will become pH-independent at higher pH. This prediction was confirmed by our experiments for this water oxidation catalyst attached to ITO

by siloxane anchor groups, where the maximum rate constant is clearly pH-independent at pH > 5.

Although this specific model is consistent with the experimental data and its prediction was validated, we cannot rule out the possibility that other models might yield similar results. In particular, the assumption of a potential-dependent $pK_{a,ox}$ has not been verified on an ITO surface. In addition, our calculations assumed that the rate constants can be described by MG theory and that the electronic coupling is the same for the ET2, EPT1, and EPT2 channels. The association equilibrium constants and reorganization energies were computed with DFT methods that also introduce some assumptions. As further experimental data become available, we will refine the assumptions used to determine the fundamental quantities as well as further test the model itself.

This general multichannel model for describing the kinetics of both homogeneous and electrochemical PCET reactions will have widespread applications. For each system, all relevant reaction channels must be identified. Then, a combination of computational and experimental data can be used to determine the various equilibrium constants and intrinsic rate constants or, in some cases, reasonable ranges for them. Within the framework of this multichannel model, analysis of the dominant forms of the redox species and the dominant channels as a function of pH will provide a deeper mechanistic understanding of PCET reactions.

■ ASSOCIATED CONTENT

Supporting Information

The Supporting Information is available free of charge at <https://pubs.acs.org/doi/10.1021/jacs.3c05535>.

Detailed derivation and analysis of the pH dependence model; validation of the equilibrium assumption of the ITO-Ru system; computational methods to estimate K_1 and K_2 ; parameters used for Figures 5, 6, and 7d; alternative fittings using different parameters; and experimental methods. The code for the kinetic model is publicly available at <https://github.com/kcui7/PCET-pH-kinetic-model> (PDF)

■ AUTHOR INFORMATION

Corresponding Author

Sharon Hammes-Schiffer – Department of Chemistry, Yale University, New Haven, Connecticut 06520, United States; orcid.org/0000-0002-3782-6995; Email: sharon.hammes-schiffer@yale.edu

Authors

Kai Cui – Department of Chemistry, Yale University, New Haven, Connecticut 06520, United States; orcid.org/0000-0001-7311-1447

Alexander V. Soudackov – Department of Chemistry, Yale University, New Haven, Connecticut 06520, United States; orcid.org/0000-0001-9581-8494

Matthew C. Kessinger – Department of Chemistry, University of North Carolina at Chapel Hill, Chapel Hill, North Carolina 27599, United States; orcid.org/0000-0002-2673-9255

Jeremiah Xu – Department of Chemistry, University of North Carolina at Chapel Hill, Chapel Hill, North Carolina 27599, United States; orcid.org/0009-0006-9579-5097

Gerald J. Meyer – Department of Chemistry, University of North Carolina at Chapel Hill, Chapel Hill, North Carolina 27599, United States; orcid.org/0000-0002-4227-6393

Complete contact information is available at: <https://pubs.acs.org/doi/10.1021/jacs.3c05535>

Notes

The authors declare no competing financial interest.

■ ACKNOWLEDGMENTS

This material is based on work solely supported as part of the Center for Hybrid Approaches in Solar Energy to Liquid Fuels (CHASE), an Energy Innovation Hub funded by the U.S. Department of Energy, Office of Science, Office of Basic Energy Sciences under award number DE-SC0021173. M.C.K. acknowledges support from an Arnold O. Beckman Postdoctoral Fellowship. The authors thank Yogi Surendranath and Jim Mayer for helpful feedback on this work.

■ REFERENCES

- (1) Hammes-Schiffer, S. Theoretical Perspectives on Proton-Coupled Electron Transfer Reactions. *Acc. Chem. Res.* **2001**, *34*, 273–281.
- (2) Mayer, J. M. Proton-Coupled Electron Transfer: A Reaction Chemist's View. *Annu. Rev. Phys. Chem.* **2004**, *55*, 363–390.
- (3) Reece, S. Y.; Nocera, D. G. Proton-Coupled Electron Transfer in Biology: Results from Synergistic Studies in Natural and Model Systems. *Annu. Rev. Biochem.* **2009**, *78*, 673–699.
- (4) Costentin, C.; Robert, M.; Savéant, J. M. Update 1 of: Electrochemical Approach to the Mechanistic Study of Proton-Coupled Electron Transfer. *Chem. Rev.* **2010**, *110*, Pr1–Pr40.
- (5) Hammes-Schiffer, S.; Stuchebrukhov, A. A. Theory of Coupled Electron and Proton Transfer Reactions. *Chem. Rev.* **2010**, *110*, 6939–6960.
- (6) Dempsey, J. L.; Winkler, J. R.; Gray, H. B. Proton-Coupled Electron Flow in Protein Redox Machines. *Chem. Rev.* **2010**, *110*, 7024–7039.
- (7) Weinberg, D. R.; Gagliardi, C. J.; Hull, J. F.; Murphy, C. F.; Kent, C. A.; Westlake, B. C.; Paul, A.; Ess, D. H.; McCafferty, D. G.; Meyer, T. J. Proton-Coupled Electron Transfer. *Chem. Rev.* **2012**, *112*, 4016–4093.
- (8) Koper, M. T. M. Theory of the Transition from Sequential to Concerted Electrochemical Proton-Electron Transfer. *Phys. Chem. Chem. Phys.* **2013**, *15*, 1399–1407.
- (9) Tyburski, R.; Liu, T.; Glover, S. D.; Hammarström, L. Proton-Coupled Electron Transfer Guidelines, Fair and Square. *J. Am. Chem. Soc.* **2021**, *143*, 560–576.
- (10) Murray, P. R. D.; Cox, J. H.; Chiappini, N. D.; Roos, C. B.; McLoughlin, E. A.; Hejna, B. G.; Nguyen, S. T.; Ripberger, H. H.; Ganley, J. M.; Tsui, E.; et al. Photochemical and Electrochemical Applications of Proton-Coupled Electron Transfer in Organic Synthesis. *Chem. Rev.* **2022**, *122*, 2017–2291.
- (11) Warburton, R. E.; Soudackov, A. V.; Hammes-Schiffer, S. Theoretical Modeling of Electrochemical Proton-Coupled Electron Transfer. *Chem. Rev.* **2022**, *122*, 10599–10650.
- (12) Costentin, C.; Robert, M.; Savéant, J. M. Concerted Proton-Electron Transfer Reactions in Water. Are the Driving Force and Rate Constant Depending on pH When Water Acts as Proton Donor or Acceptor? *J. Am. Chem. Soc.* **2007**, *129*, 5870–5879.
- (13) Renger, G.; Christen, G.; Karge, M.; Eckert, H. J.; Irrgang, K. D. Application of the Marcus theory for analysis of the temperature dependence of the reactions leading to photosynthetic water oxidation: results and implications. *JBC, J. Biol. Inorg. Chem.* **1998**, *3*, 360–366.
- (14) Sjödin, M.; Styring, S.; Akerman, B.; Sun, L. C.; Hammarström, L. Proton-Coupled Electron Transfer from Tyrosine

in a Tyrosine-Ruthenium-tris-bipyridine Complex: Comparison with Tyrosine(z) Oxidation in Photosystem II. *J. Am. Chem. Soc.* **2000**, *122*, 3932–3936.

(15) Irebo, T.; Reece, S. Y.; Sjodin, M.; Nocera, D. G.; Hammarström, L. Proton-Coupled Electron Transfer of Tyrosine Oxidation: Buffer Dependence and Parallel Mechanisms. *J. Am. Chem. Soc.* **2007**, *129*, 15462–15464.

(16) Zhang, M. T.; Hammarström, L. Proton-Coupled Electron Transfer from Tryptophan: A Concerted Mechanism with Water as Proton Acceptor. *J. Am. Chem. Soc.* **2011**, *133*, 8806–8809.

(17) Bonin, J.; Costentin, C.; Robert, M.; Routier, M.; Savéant, J. M. Proton-Coupled Electron Transfers: pH-Dependent Driving Forces? Fundamentals and Artifacts. *J. Am. Chem. Soc.* **2013**, *135*, 14359–14366.

(18) Nilsen-Moe, A.; Rosichini, A.; Glover, S. D.; Hammarström, L. Concerted and Stepwise Proton-Coupled Electron Transfer for Tryptophan-Derivative Oxidation with Water as the Primary Proton Acceptor: Clarifying a Controversy. *J. Am. Chem. Soc.* **2022**, *144*, 7308–7319.

(19) Kessinger, M.; Soudackov, A. V.; Schneider, J.; Bangle, R. E.; Hammes-Schiffer, S.; Meyer, G. J. Reorganization Energies for Interfacial Proton-Coupled Electron Transfer to a Water Oxidation Catalyst. *J. Am. Chem. Soc.* **2022**, *144*, 20514–20524.

(20) Laviron, E. Theoretical-Study of a $1e$, $1H^+$ Surface Electrochemical Reaction (4-Member Square Scheme) When the Protonation Reactions Are at Equilibrium. *J. Electroanal. Chem.* **1980**, *109*, 57–67.

(21) Finklea, H. O. Theory of Coupled Electron-Proton Transfer with Potential-Dependent Transfer Coefficients for Redox Couples Attached to Electrodes. *J. Phys. Chem. B* **2001**, *105*, 8685–8693.

(22) Lewis, N.; Bisbey, R.; Westendorff, K.; Soudackov, A. V.; Surendranath, Y. A Molecular-Level Mechanistic Framework for Interfacial Proton Coupled Electron Transfer Kinetics. *ChemRxiv*, May 08, **2023**, DOI: 10.26434/chemrxiv-2023-lc7d9-v2 (accessed May 20, 2023).

(23) Su, L.; Chen, J.; Yang, F.; Li, P.; Jin, Y.; Luo, W.; Chen, S. Electric-Double-Layer Origin of the Kinetic pH Effect of Hydrogen Electrocatalysis Revealed by a Universal Hydroxide Adsorption-Dependent Inflection-Point Behavior. *J. Am. Chem. Soc.* **2023**, *145*, 12051–12058.

(24) Schmickler, W.; Santos, E. *Interfacial Electrochemistry*, 2nd ed.; Springer, 2010.

(25) Savéant, J. M.; Costentin, C. *Elements of Molecular and Biomolecular Electrochemistry: An Electrochemical Approach to Electron Transfer Chemistry*, 2nd ed.; John Wiley & Sons, Ltd., 2019.

(26) Soudackov, A.; Hammes-Schiffer, S. Multistate Continuum Theory for Multiple Charge Transfer Reactions in Solution. *J. Chem. Phys.* **1999**, *111*, 4672–4687.

(27) Hammes-Schiffer, S.; Soudackov, A. V. Proton-Coupled Electron Transfer in Solution, Proteins, and Electrochemistry. *J. Phys. Chem. B* **2008**, *112*, 14108–14123.

(28) Venkataraman, C.; Soudackov, A. V.; Hammes-Schiffer, S. Theoretical Formulation of Nonadiabatic Electrochemical Proton-Coupled Electron Transfer at Metal-Solution Interfaces. *J. Phys. Chem. C* **2008**, *112*, 12386–12397.

(29) Hammes-Schiffer, S. Proton-Coupled Electron Transfer: Moving Together and Charging Forward. *J. Am. Chem. Soc.* **2015**, *137*, 8860–8871.

(30) Lindquist, R.; Rawn, J. D. *Problems and Solutions Guide to Accompany Rawn Biochemistry*; N. Patterson Publishers, 1990.

(31) Elgrishi, N.; Rountree, K. J.; McCarthy, B. D.; Rountree, E. S.; Eisenhart, T. T.; Dempsey, J. L. A Practical Beginner's Guide to Cyclic Voltammetry. *J. Chem. Educ.* **2018**, *95*, 197–206.

(32) Marcus, R. A. On Theory of Electron-Transfer Reactions. 6. Unified Treatment for Homogeneous and Electrode Reactions. *J. Chem. Phys.* **1965**, *43*, 679.

(33) Chidsey, C. E. D.; Bertozzi, C. R.; Putvinski, T. M.; Muijsce, A. M. Coadsorption of Ferrocene-Terminated and Unsubstituted

Alkanethiols on Gold: Electroactive Self-Assembled Monolayers. *J. Am. Chem. Soc.* **1990**, *112*, 4301–4306.

(34) Zeng, Y.; Smith, R. B.; Bai, P.; Bazant, M. Z. Simple formula for Marcus-Hush-Chidsey kinetics. *J. Electroanal. Chem.* **2014**, *735*, 77–83.

(35) Farnum, B. H.; Morseth, Z. A.; Brennaman, M. K.; Papanikolas, J. M.; Meyer, T. J. Application of Degenerately Doped Metal Oxides in the Study of Photoinduced Interfacial Electron Transfer. *J. Phys. Chem. B* **2015**, *119*, 7698–7711.

(36) Soudackov, A.; Hammes-Schiffer, S. Derivation of Rate Expressions for Nonadiabatic Proton-Coupled Electron Transfer Reactions in Solution. *J. Chem. Phys.* **2000**, *113*, 2385–2396.

(37) Trammell, S. A.; Wimbish, J. C.; Odobel, F.; Gallagher, L. A.; Narula, P. M.; Meyer, T. J. Mechanisms of Surface Electron Transfer. Proton-Coupled Electron Transfer. *J. Am. Chem. Soc.* **1998**, *120*, 13248–13249.

(38) Concepcion, J. J.; Jurss, J. W.; Norris, M. R.; Chen, Z. F.; Templeton, J. L.; Meyer, T. J. Catalytic Water Oxidation by Single-Site Ruthenium Catalysts. *Inorg. Chem.* **2010**, *49*, 1277–1279.

(39) Wasylenko, D. J.; Ganesamoorthy, C.; Henderson, M. A.; Koivisto, B. D.; Osthoff, H. D.; Berlinguette, C. P. Electronic Modification of the $[Ru-II(tpy)(bpy)(OH_2)]^{2+}$ Scaffold: Effects on Catalytic Water Oxidation. *J. Am. Chem. Soc.* **2010**, *132*, 16094–16106.

(40) Boyer, J. L.; Polyansky, D. E.; Szalda, D. J.; Zong, R. F.; Thummel, R. P.; Fujita, E. Effects of a Proximal Base on Water Oxidation and Proton Reduction Catalyzed by Geometric Isomers of $[Ru(tpy)(pynap)(OH_2)]^{2+}$. *Angew. Chem., Int. Ed.* **2011**, *50*, 12600–12604.

(41) Asaduzzaman, A. M.; Wasylenko, D.; Berlinguette, C. P.; Schreckenbach, G. Substitution Effects on the Water Oxidation of Ruthenium Catalysts: A Quantum-Chemical Look. *J. Phys. Chem. C* **2015**, *119*, 242–250.

(42) Duffy, E. M.; Marsh, B. M.; Garand, E. Probing the Hydrogen-Bonded Water Network at the Active Site of a Water Oxidation Catalyst: $[Ru(bpy)(tpy)(H_2O)]^{2+}(H_2O)_{0-4}$. *J. Phys. Chem. A* **2015**, *119*, 6326–6332.

(43) Duffy, E. M.; Marsh, B. M.; Voss, J. M.; Garand, E. Characterization of the Oxygen Binding Motif in a Ruthenium Water Oxidation Catalyst by Vibrational Spectroscopy. *Angew. Chem., Int. Ed.* **2016**, *55*, 4079–4082.

(44) Ravari, A. K.; Zhu, G. B.; Ezhov, R.; Pineda-Galvan, Y.; Page, A.; Weinschenk, W.; Yan, L. F.; Pushkar, Y. Unraveling the Mechanism of Catalytic Water Oxidation via de Novo Synthesis of Reactive Intermediate. *J. Am. Chem. Soc.* **2020**, *142*, 884–893.

(45) Ge, A. M.; Kastlunger, G.; Meng, J. H.; Lindgren, P.; Song, J.; Liu, Q. L.; Zaslavsky, A.; Lian, T. Q.; Peterson, A. A. On the Coupling of Electron Transfer to Proton Transfer at Electrified Interfaces. *J. Am. Chem. Soc.* **2020**, *142*, 11829–11834.

(46) Bel Hadj Tahar, R.; Ban, T.; Ohya, Y.; Takahashi, Y. Tin Doped Indium Oxide Thin Films: Electrical Properties. *J. Appl. Phys.* **1998**, *83*, 2631–2645.

(47) Minami, T. Transparent Conducting Oxide Semiconductors for Transparent Electrodes. *Semicond. Sci. Technol.* **2005**, *20*, S35–S44.

(48) Huber, F. L.; Wernbacher, A. M.; Perleth, D.; Nauroozi, D.; Gonzalez, L.; Rau, S. A Ruthenium(II) Water Oxidation Catalyst Containing a pH-Responsive Ligand Framework. *Inorg. Chem.* **2021**, *60*, 13299–13308.

(49) Materna, K. L.; Crabtree, R. H.; Brudvig, G. W. Anchoring Groups for Photocatalytic Water Oxidation on Metal Oxide Surfaces. *Chem. Soc. Rev.* **2017**, *46*, 6099–6110.

(50) Ardo, S.; Achey, D.; Morris, A. J.; Abrahamsson, M.; Meyer, G. J. Non-Nernstian Two-Electron Transfer Photocatalysis at Metalloporphyrin-TiO₂ Interfaces. *J. Am. Chem. Soc.* **2011**, *133*, 16572–16580.

(51) Bisquert, J.; Fabregat-Santiago, F.; Mora-Sero, I.; Garcia-Belmonte, G.; Barea, E. M.; Palomares, E. A Review of Recent Results on Electrochemical Determination of the Density of Electronic States

of Nanostructured Metal-Oxide Semiconductors and Organic Hole Conductors. *Inorg. Chim. Acta* **2008**, 361, 684–698.

(52) Nelsen, S. F.; Blackstock, S. C.; Kim, Y. Estimation of Inner Shell Marcus Terms for Amino Nitrogen-Compounds by Molecular-Orbital Calculations. *J. Am. Chem. Soc.* **1987**, 109, 677–682.

(53) Auer, B.; Fernandez, L. E.; Hammes-Schiffer, S. Theoretical Analysis of Proton Relays in Electrochemical Proton-Coupled Electron Transfer. *J. Am. Chem. Soc.* **2011**, 133, 8282–8292.